

Cloud three-dimensional effects evidenced in Landsat spatial power spectra and autocorrelation functions

Lazaros Oreopoulos, Alexander Marshak, Robert F. Cahalan, and Guoyong Wen

Climate and Radiation Branch, NASA Goddard Space Flight Center, Greenbelt, Maryland
Joint Center for Earth Systems Technology, University of Maryland Baltimore County, Baltimore

Abstract. An analysis of nadir reflectivity spatial Fourier power spectra and autocorrelation functions for solar wavelengths and cloudy conditions is presented. The data come from Landsat thematic mapper (TM) observations, while Monte Carlo (MC) simulations are used to aid the interpretation of the observations and to examine sensitivity to various factors. We show that shortwave radiative processes produce consistent signatures in power spectra and autocorrelation functions. Power spectra take a variety of shapes not shown or explained in previous observational studies. We demonstrate that TM spectra can potentially be affected by radiative “roughening” at intermediate scales ($\sim 1\text{--}5$ km) and radiative “smoothing” at small scales (<1 km). These processes are wavelength-dependent, with systematic differences between conservative (for cloud droplets) TM band 4 (~ 0.8 μm) and absorbing band 7 (~ 2.2 μm). Band 7 exhibits more roughening and less smoothing than band 4 and faster decrease in autocorrelation. Roughening is more prevalent at large solar zenith angles due to optical and/or geometrical side illumination and shadowing. MC spectra illustrate that scale invariant optical depth fields can produce complex power spectra that take a variety of shapes under different conditions. Radiative roughening increases with decreasing single scattering albedo and increasing solar zenith angle (as in the observations). For low solar zenith angles, there is a clear shift in the radiative smoothing scale to smaller values as droplet absorption increases. Power spectra also show stronger decorrelations between optical depth and reflectivity when cloud top variations are more pronounced. Finally, it is shown that power spectral analysis is a useful tool for evaluating the skill of novel optical depth retrieval techniques in removing three-dimensional radiative effects. New techniques using inverse nonlocal independent pixel approximation and normalized difference of nadir reflectivity yield optical depth fields which better match the scale-by-scale variability of the true optical depth field.

1. Introduction

In recent years, with the steady increase in the spatial resolution of satellite radiometers the role of three-dimensional (3-D) radiative transfer in the appearance of clouds from space has been well recognized [e.g., *Wielicki et al.*, 1995; *Barker and Liu*, 1995; *Chambers et al.*, 1997; *Davis et al.*, 1997; *Oreopoulos et al.*, 2000]. Although there are indications that even at coarse resolutions (~ 30 km) such as those of the Earth Radiation Budget Experiment (ERBE) 3-D effects are detectable [*Loeb and Davies*, 1996], it seems that the most appropriate data sets to study errors from the use of plane-parallel inversion algorithms are those coming from a high spatial resolution sensor such as the Thematic Mapper (TM) aboard the Landsat series of satellites (~ 30 m spatial resolution). While Landsat scene prices (especially prior to Landsat 7), high storage volume, and scarcity of certain types of cloudy scenes (such as marine clouds) impose practical limitations, there is the benefit of being able to more confidently detect 3-D radiative processes. This is because Landsat resolves scales smaller than typical photon mean free paths [*Marshak et al.*, 1998b] where the assumption of no net horizontal exchange of photons between

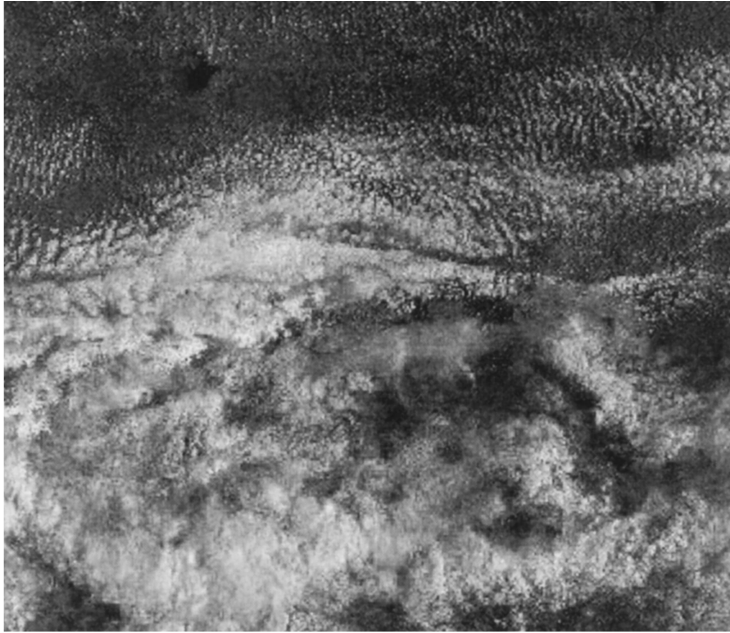
cloudy columns, known as independent pixel approximation (IPA), is no longer valid [*Cahalan et al.*, 1994].

One example of the sensitivity of Landsat to radiative processes unresolved by other instruments is scale breaks (steepening of log-log slopes) detected in spatial Fourier power spectra of conservative TM bands [*Cahalan and Snider*, 1989; *Marshak et al.*, 1995] at small scales. These were shown to be caused by radiative smoothing due to multiple scattering [*Davis et al.*, 1997]. The location of the break provides information for approximating the radiative Green's function which is used in the IPA extension known as nonlocal independent pixel approximation (NIPA) [*Marshak et al.*, 1995] and has been linked to the geometrical and optical thickness of clouds [*Marshak et al.*, 1995; *Davis et al.*, 1997]. Alternative interpretations to scale breaks appearing in coarser resolution advanced very high resolution radiometer (AVHRR) spectra were presented by *Barker and Davies* [1992].

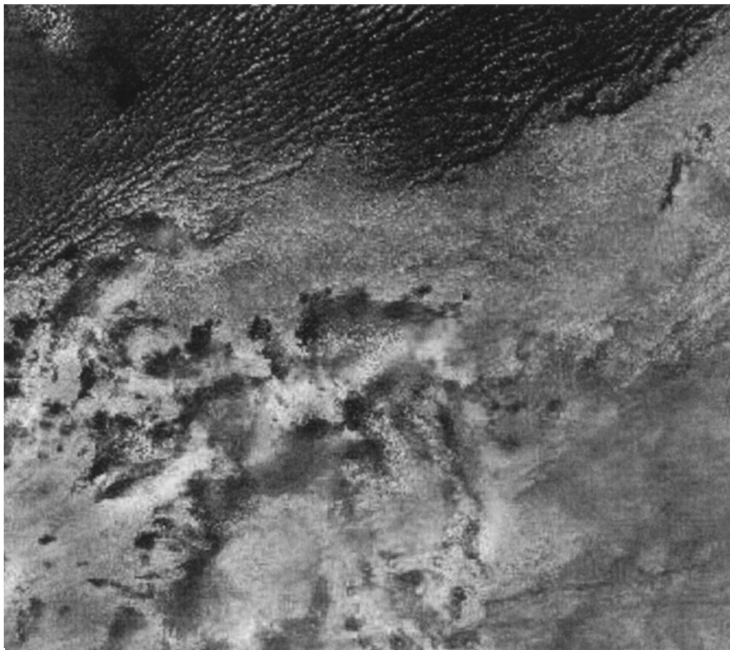
By relating scale breaks with radiative smoothing, power spectra become a useful tool for deducing the physical, scaling, and radiative properties of clouds. Can this relation be also extended to power spectra of absorptive (with respect to non-gaseous water) wavelengths? Intuitively, one expects photon trajectories to be more localized at absorbing wavelengths and less radiative smoothing to take place. Does this manifest itself as a shift in the location of the scale break toward smaller scales? There is also the issue of intermediate-scale roughen-

Copyright 2000 by the American Geophysical Union.

Paper number 2000JD900153.
0148-0227/00/2000JD900153\$09.00



(a)



(b)

Figure 1. Visible images of the two Landsat 5 TM scenes used in the study: (a) scene 1 and (b) scene 2.

ing due to low-order scattering at oblique illumination angles seen in the 3-D simulations of *Zuidema and Evans* [1998] and *Várnai* [2000]. Is this also observed in Landsat power spectra and is it more or less prominent for absorptive bands? Results that help answer these questions are presented in this work, which for the first time compiles and processes in a consistent manner a large ensemble of spatial power spectra and their Fourier transforms, namely, spatial autocorrelation functions.

After a description of the data set and analysis method in section 2, Landsat results are presented in section 3, while results from Monte Carlo (MC) radiative transfer simulations follow in section 4. Examples of using power spectra to evaluate optical depth retrievals are given in section 5. Finally,

results are summarized and general conclusions are drawn in section 6.

2. Data Set and Methodology

We have used two Landsat 5 scenes over the atmospheric radiation measurement (ARM) program southern Great Plains site in Oklahoma ($\sim 36.6^\circ\text{N}$, 97.5°W). The scenes are shown in Figure 1, and information is given in Table 1. Each scene is divided into 25 subscenes of 1024×1024 pixels, with a nominal resolution of 28.5 m, for which Fourier spatial power spectra (power spectral densities) and spatial autocorrelation functions are calculated. The partition of the two scenes into

Table 1. Information on the Two Landsat 5 TM Scenes Used in This Study

Name	Acquisition Date	Size, pixels	CF	$\langle R_4 \rangle$	SZA
Scene 1	July 20, 1995	6477 × 6860	0.805	0.437	34°
Scene 2	Sept. 24, 1996	6489 × 6888	0.870	0.571	45°

CF is the cloud fraction of the scene (number of pixels classified as cloudy by a threshold algorithm over the total number of pixels) and $\langle R_4 \rangle$ is the mean band 4 reflectivity defined as $\pi I_4 / (\mu_0 F_4)$, where μ_0 is the cosine of the solar zenith angle (SZA), I_4 is the nadir radiance, and F_4 is the extraterrestrial solar flux for band 4.

50 subscenes allows examination of differences among the power spectra which can be related to regional features. The results in the following are from 1-D average spectra and autocorrelations of the band 4 (B_4) and band 7 (B_7) nadir reflectivities (R_4 and R_7 , respectively). The central wavelengths of these bands are ~ 0.83 and $2.2 \mu\text{m}$, respectively. These bands were chosen because of the substantial difference in their droplet absorption (single scattering albedo $\omega_0 = 1$ for B_4 and $\omega_0 \approx 0.98$ for $10\text{-}\mu\text{m}$ droplets in the center of B_7). We have verified that the average 1-D spectra are very similar to the (computationally more expensive) 2-D spectra, indicating that our scenes possess a good degree of isotropy. Spectral densities are calculated as the mean square amplitudes of the Fourier coefficients, while the autocorrelation function at lag r (distance corresponding to integer multiples of 28.5 m) is calculated as an average of

$$\alpha(r) = \frac{\sum_n [R_i(x_n + r) - \langle R_i \rangle][R_i(x_n) - \langle R_i \rangle]}{\sum_n [R_i(x_n) - \langle R_i \rangle]^2}, \quad (1)$$

where $i = 4$ or 7 is the TM band index, $R_i(x_n)$ is the reflectivity at the pixel with (arbitrary) coordinate x_n , and $\langle R_i \rangle$ is the mean reflectivity of the 1024-pixel strip.

In many instances, power spectra are compared via their slopes in log-log plots calculated by least squares linear regression (assuming that the spectra approach power law behavior, i.e., $E(k) = Ck^{-\beta}$):

$$\log E(k) = \gamma - \beta \log k, \quad (2)$$

where $E(k)$ is the power spectral density, k is the wavenumber (inverse distance), $\gamma = \log C$, and β is the spectral exponent (slope in a log-log plot). See *Davis et al.* [1996, Appendix A] for details. Regression can be performed either over all scales (single fit) or separately over chosen scaling ranges (i.e., “large scales,” “small scales,” “intermediate scales,” somewhat loosely defined) since, as will be shown later, the frequent violation of scale invariance makes spectral slopes change over the scales considered.

We also perform spectral analysis on nadir reflectivities produced by MC simulations on several incarnations of 1-D fractal clouds produced by the bounded cascade model of *Cahalan et al.* [1994]. The various incarnations represent clouds with varying characteristics such as mean optical depth $\langle \tau \rangle$, cloud top height variability, mean cloud geometrical thickness $\langle h \rangle$, etc. The parameter values for the various cases will be given in the captions of the figures where the relevant results are presented. To avoid the noise due to the limited number of realizations (10) for each experiment, we work with ensemble average octave-wide binned spectra [*Davis et al.*, 1996]. The 1-D clouds consist of 1024 columns that are 25 m wide in the horizontal but have, in general, variable vertical extent. The MC simula-

tions were performed for several single scattering albedos, using a Henyey-Greenstein phase function with asymmetry factor $g = 0.85$ (tests with a detailed Mie phase function showed that there are no qualitative differences in the behavior of the power spectra). The number of photons used per simulation was 2×10^8 ; such a large number was deemed necessary to achieve small nadir reflectivity errors ($< 1\%$) at the pixel level. No clear-sky atmospheric effects were accounted for in these MC simulations.

The octave-binned MC spectra have only a few points (nine), so slope comparisons from dual regressions on small and large scales are less reliable than in Landsat. We found that in addition to the subjective visual comparison, a measure of spectra differences can be attained by plotting pairs of spectra versus one another and calculating slope ratios by least squares regression. This is possible for two power spectra $E_1 = C_1 k^{-\beta_1}$ and $E_2 = C_2 k^{-\beta_2}$ since it can be shown that they are related as in

$$E_2 = CE_1^{\beta_2/\beta_1}, \quad (3)$$

where $C = C_2 C_1^{-\beta_2/\beta_1}$. Thus, in a log-log plot of E_2 versus E_1 the slope of the linear fit would provide approximate values of β_2/β_1 and hence a measure of relative steepness (for easier comparisons we can force the diagonal of the plot to be the $\beta_2/\beta_1 = 1$ line by having equal number of decades on both axes). In the presence of scale breaks, there may be two or more regimes with different β_2/β_1 values. Single fits over the entire range of scales are sufficient to draw conclusions in many cases, but we occasionally also apply the fit on only the last five octave points (< 1 km), with the understanding that the results should be treated with caution. Note that the spatial scales in such $\log E_2$ versus $\log E_1$ plots can be identified from their monotonic association with spectral power (small scales have less power than large scales).

3. Observations

3.1. The Great Variety of Cloudy Spectra

Figure 2 is a selection of observed nadir radiance power spectra from the two Landsat scenes. These spectra are constructed from B_4 and B_7 raw counts and correspond to 1024×1024 subscenes, giving a range of scales from ~ 60 m to ~ 30 km. One sees that the power spectra can take a variety of shapes that are in many instances wavelength-dependent. Radiative smoothing (steepening of slopes, indicating weaker fluctuations) is present at small scales in all cases except perhaps Figure 2a, sometimes accompanied by definite radiative roughening (flattening of slopes due to stronger fluctuations) at intermediate scales (Figures 2d and 2e). One case (Figure 2a) approaches near scale invariance (constant slope throughout the whole range of scales). Interestingly, the spectra of the two bands differ only above ~ 0.4 km for Figure 2b, while the

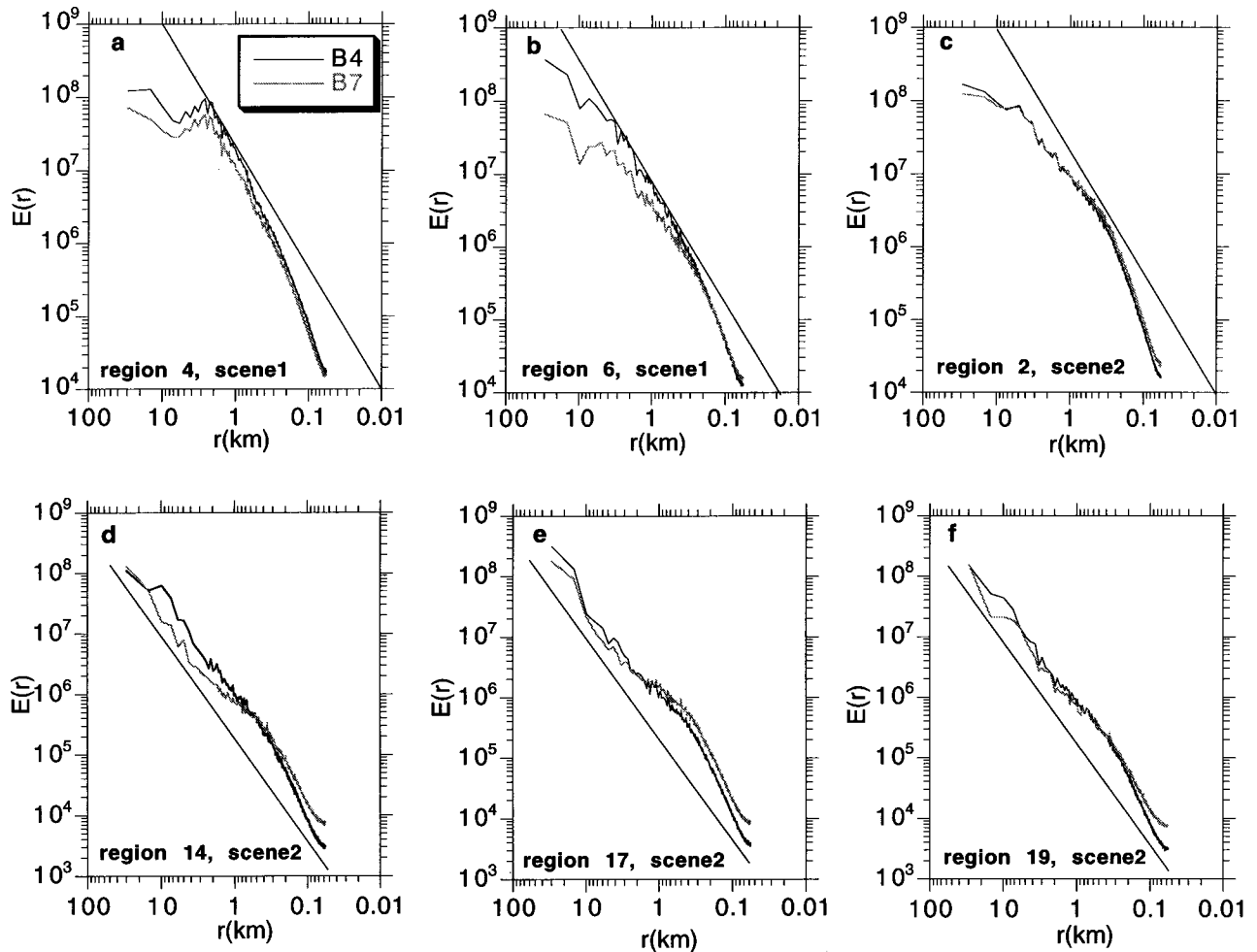


Figure 2. Fourier spectral densities for select 1024×1024 pixel regions taken from the two Landsat scenes. Spectra are shown for TM bands 4 (B_4) and 7 (B_7). The straight line has a slope of $5/3$ and aids in the visual comparison of the spectra for the two bands.

spectra are virtually identical at all scales for Figure 2c. Finally, Figure 2f shows a different degree of radiative smoothing for the two bands at small scales (below ~ 0.3 km), while there is roughening with comparable slopes at large scales. Some notable links between the form of the spectra and properties of the scene or subscene are as follows:

1. The absence of radiative roughening in Figures 2a and 2b, as well as other power spectra from scene 1 (not shown here), is consistent with the lower solar zenith angle (SZA) for this scene ($SZA = 34^\circ$ versus 45° for scene 2). This is also shown later in MC simulations.

2. The weak radiative smoothing when clouds are thin (Figure 2a with $\langle R_4 \rangle = 0.36$ compared to 0.60 for Figure 2b) is consistent with reduced multiple scattering in clouds.

3. The close proximity of the spectra (Figure 2c) is consistent with B_7 reflectivities approaching B_4 reflectivities ($\langle R_7 \rangle = 0.33$ and $\langle R_4 \rangle = 0.39$) in a region with a significant clear sky fraction ($\sim 25\%$).

4. The appearance of radiative roughening is commensurate with thick ($\langle R_4 \rangle = 0.66$ and $\langle R_4 \rangle = 0.68$ for Figures 2d and 2e, respectively) overcast clouds having significant cloud top variability (standard deviations of B_6 brightness temperature ~ 5 – 6 K compared to ~ 3 K or lower for, e.g., Figure 2c and other subscenes with less spectral flattening) and is wave-

length-dependent, also consistent with MC simulations shown later.

The above compilation of reflectivity spectra therefore suggests that the inherent variety of shapes is related to 3-D radiative transfer (the relevant processes will be described in section 4.1 in more detail with the aid of MC simulations) and that difficulties in their systematic and quantitative cross comparison should be anticipated. On the other hand, it also illustrates that information on cloud characteristics and structure may be obtained from analyzing power spectra.

3.2. Wavelength Dependence

Given the complexity of power spectra, it is difficult to quantify the systematic differences within a large ensemble. In this paper, we compare spectra by their slopes derived from regression analysis as explained in section 2. Spectral slopes allow us to draw conclusions on the degree of smoothing or roughening of the radiation field, as pointed out in the section 3.1. In this section we compare regression slopes for TM B_4 and B_7 , by either performing single fits (entire spatial range) or double fits (separate for large and small scales). The single fits, giving an “effective” slope, are obviously a crude approximation given the complexity of the spectra but are nevertheless capable of capturing systematic dependencies. The two-fit procedure is

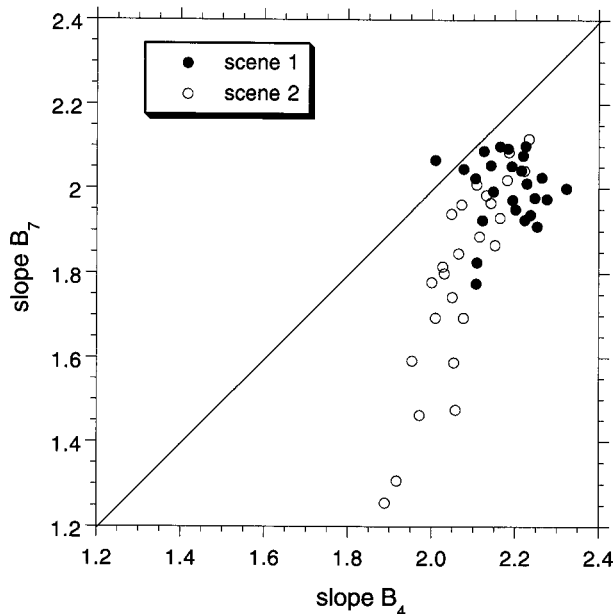


Figure 3. Comparison of power spectra slopes for TM bands 4 and 7 derived from single regression fits according to equation (2) for fifty 1024×1024 pixel regions from the two Landsat scenes.

also not perfect, the most apparent weakness being the disproportionate number of points for the two scaling ranges: the fit before the break (large and intermediate scales) is calculated from a small number of points, while the small-scale fit is calculated from a large number of points. We note that *Oreopoulos et al.* [1999] have presented a two-fit procedure which also attempted to detect the location of the break based on various criteria. These criteria were satisfied in only about half the cases, while yielding similar results with respect to regression slopes as here.

Figure 3 compares the spectral slopes between B_4 and B_7 when a single fit is applied. B_7 slopes are systematically smaller (i.e., the corresponding fields rougher) than B_4 . This conforms with our expectation that photons with a greater chance of getting absorbed (B_7 photons) travel smaller distances and are thus less effective in smoothing out optical depth gradients. Another notable characteristic of Figure 3 is that scene 2, which is illuminated by a lower Sun ($SZA = 45^\circ$ versus 34° for scene 1), shows a greater range of B_7 slopes, suggesting that at low illumination the absorbing band is more sensitive to the low-order scattering events of cloud geometry (bumps, edges, gaps, etc.) that cause roughening.

Figure 4 compares the two-fit slopes for large (understood to comprise everything that is not small) scales (Figure 4a), and small scales (Figure 4b), with either 0.5 or 1 km used as the distance (r_b) separating the two regimes. Again, B_4 slopes are systematically larger than B_7 slopes at all scales. The large-scale slopes for B_4 have their highest concentration around the $5/3$ slope predicted by turbulence theory for a passive scalar [Cahalan and Snider, 1989], while the small-scale slopes are mostly between 2.2 and 2.8. The greater proximity to the diagonal for large scales compared to small scales for scene 2 suggests that for lower Sun the wavelength-dependent contrast between small and large scales becomes stronger and that the single fit results of Figure 3 are largely driven by the behaviour at small scales (notice the similarity in Figures 3 and 4b).

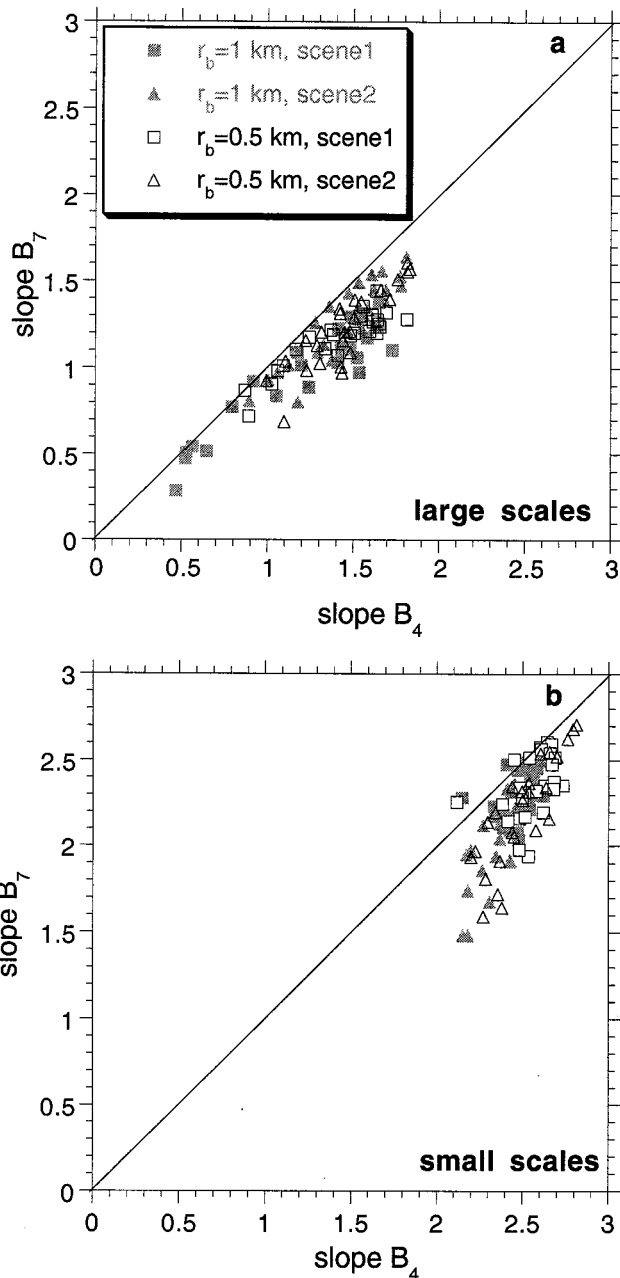


Figure 4. Comparison of power spectra slopes for TM B_4 and B_7 derived from linear regression, separately for (b) small $r < r_b$ and (a) large $r > r_b$ scales, where $r_b = 0.5$ km or $r_b = 1$ km. Same data as in Figure 3 were used.

Finally, while the details of defining the scale length that separates large and small scales do not affect the conclusions of this exercise, we note that for both bands the small-scale slopes are systematically steeper for $r_b = 0.5$ km compared to $r_b = 1$ km, but this distinction is less clear for large-scale slopes (not shown).

3.3. Autocorrelation Functions

The power spectra signatures indicating the different nature of 3-D radiative transfer for absorbing and nonabsorbing wavelengths are expected to also appear in spatial autocorrelation functions. Figure 5 confirms this. Both the value of the autocorrelation coefficient at a fixed lag of 10 pixels (~ 300 m) (Figure 5a) and the scale length (or decorrelation length, the

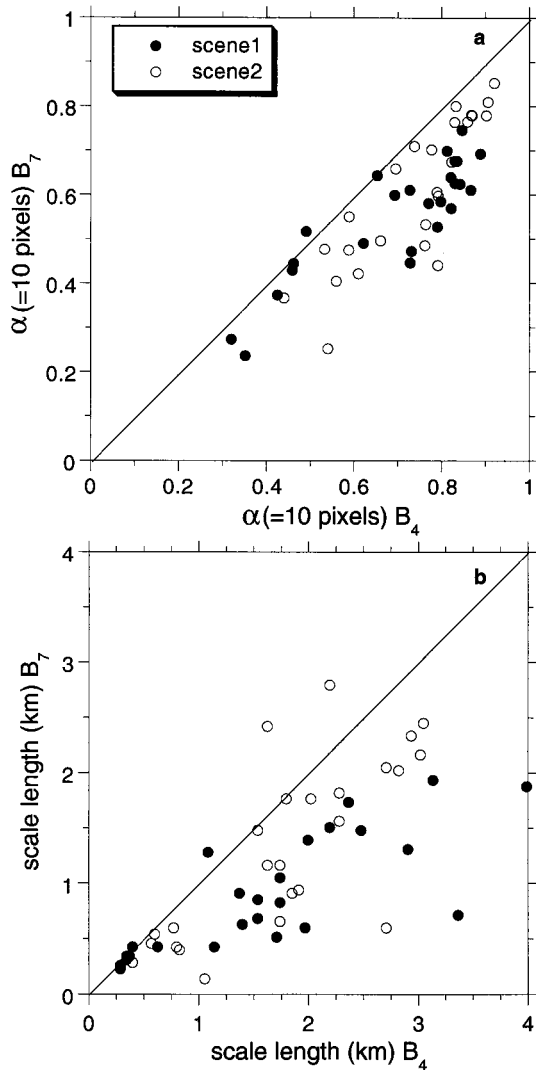


Figure 5. B_4 and B_7 comparison (a) of autocorrelation function values at a fixed lag of 10 pixels (~ 300 m) and (b) of autocorrelation function scale lengths (distance where autocorrelation drops to $1/e$) in km. Same data as in Figure 3 were used.

distance where the value of the autocorrelation function drops to $1/e$) (Figure 5b) are at most times larger for B_4 than B_7 and thus are consistent with the power spectra regression results. The two scene 2 points far above the diagonal belong to regions 14 and 19 and have length scales in the neighborhood where roughening is more prevalent (Figures 2d and 2f), indicating that perhaps length scales are not as robust as autocorrelations at short lags in characterizing smoothing. Points along the diagonal with small decorrelation lengths belong to thin clouds with little multiple scattering. Figure 5 is in general accordance with 3-D radiative transfer considerations: photons with no chance of being absorbed by cloud droplets traverse larger distances and experience more scattering events before exiting the cloud, thus smoothing the field of reflected radiation. The above results are also in agreement with the wavelength dependency of root-mean-square (rms) horizontal photon displacement shown by Platnick [2000] and the theoretical diffusion results developed by A. Davis and A. Marshak (Multiple scattering in clouds: Insights from three-dimensional dif-

fusion/P1 theory, submitted to *Nuclear Science Engineering*, 2000).

4. Simulations

MC simulations provide spectra from experiments under controlled conditions. Therefore changes in spectra can be traced back to changes in cloud characteristics and/or external factors. Ultimately, we want to use the experience gained by examining MC spectra to identify cloud characteristics in the observed spectra (as attempted in section 3.1.). This goal can be achieved only if simulated MC spectra have a good degree of realism and bear qualitative resemblance to observations. In the following, we will demonstrate that MC spectra do indeed share many of the properties of observed spectra.

4.1. Effect of Single Scattering Albedo and Solar Zenith Angle

The observed Landsat radiance spectra of section 3 showed a consistent dependency on wavelength: the spectral slopes of conservative B_4 were steeper (i.e., the radiation field was smoother) than absorbing B_7 slopes at all scales. This finding is confirmed by the MC simulations. Figure 6 shows scatterplots of $E(k)$ for $\omega_0 = 0.98$ versus $E(k)$ for $\omega_0 = 1$ for both IPA and MC calculations on flat cascade clouds under illumination conditions close to those of the TM observations, i.e., $\text{SZA} = 30^\circ$ (Figure 6a) and $\text{SZA} = 45^\circ$ (Figure 6b). While the arrangement of points is parallel to the diagonal ($\beta_2/\beta_1 \approx 1$, in equation (3)) for IPA calculations (performed with the DISORT model of Stamnes *et al.* [1988]), with individual slopes equal to the slope of the optical depth field spectrum (see Figure 7), for MC it suggests ratio of slopes $\beta_2/\beta_1 < 1$, particularly at small scales, as in the observations (Figure 4b). Thus the IPA spectra remain scale invariant as absorption increases, but the MC spectra do not. The disparity in slopes between the absorptive and nonabsorptive cases increases with SZA. For example, a single fit to the data of Figure 6 gives slope ratios of 0.87 and 0.84 for $\text{SZA} = 30^\circ$ and $\text{SZA} = 45^\circ$, respectively, with deviations from scale invariance starting earlier (larger scales) for $\text{SZA} = 45^\circ$. Slope disparity further increases when cloud top variability is added to the cascade clouds (see Figure 8).

The shift in the location of the break point (distance at which radiative smoothing commences) to smaller scales and the reduction in the small-scale slope as single scattering albedo decreases in our MC simulations are clearly illustrated in Figure 7. We use single scattering albedos $\omega_0 = 1, 0.98$, and 0.95 and include the power spectra of IPA nadir reflectivity. These spectra are scale invariant with scaling exponent close to that for the optical depth spectra [Davis *et al.*, 1997] and provide a nice reference for visualizing the translation of the breaking point to smaller values and the flattening of small-scale slopes as ω_0 decreases. We attribute these changes to the more localized nature of photon exchange between cloudy columns in the presence of absorption, resulting in weaker radiative smoothing. However, the downward shift of break location becomes less clear as SZA increases and roughening begins to occur. The $\text{SZA} = 0^\circ$ and 30° spectra have considerably less roughening at intermediate scales, thus following better the two-regime (i.e., only smoothing at small scales) power spectra model that has been frequently presented in the literature [e.g., Cahalan and Snider, 1989; Marshak *et al.*, 1995; Davis *et al.*, 1997]. However, for $\text{SZA} = 45^\circ$ or 60° the two-regime model becomes inadequate, more so for variable cloud

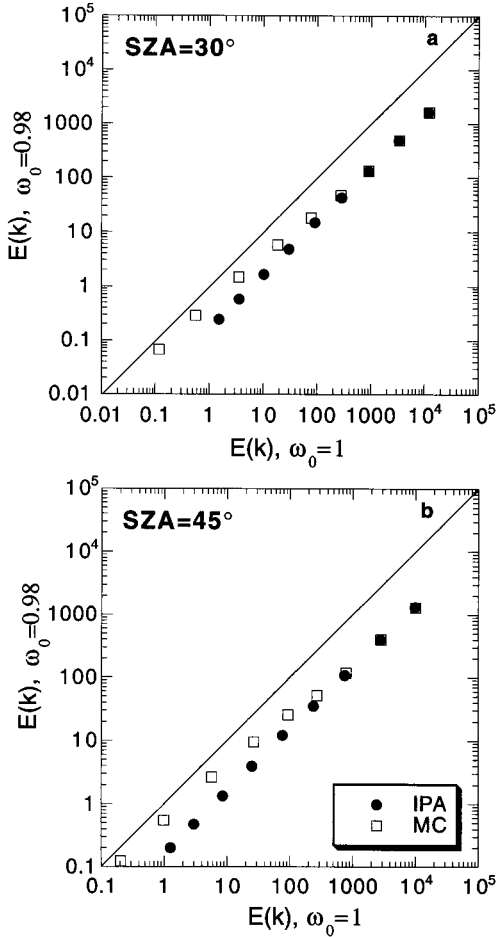


Figure 6. Scatterplot of $\log E$ versus $\log E$ octave-binned spectral power for two single scattering albedos, derived from IPA and MC simulations. A 1024-column bounded cascade was used with flat base and top, mean geometrical thickness $h = 0.3$ km, variance parameter $p = 0.4$, and scaling parameter $H = 0.33$. Surface is black and there is no atmosphere. Results are shown for (a) $\text{SZA} = 30^\circ$ and (b) $\text{SZA} = 45^\circ$.

top clouds (see section 4.2) and absorbing wavelengths. Thus, while smoothing at small scales happens for all cloud types and solar zenith angles, it is often masked by optical and/or geometrical side illumination and shadowing produced by intermediate-scale variability. In summary, nadir reflectivity spectra for these MC experiments are generally characterized by three distinct regimes: (1) large scales ($> \sim 5$ km or $10\text{--}15 \langle h \rangle$), where reflectivity follows fluctuations of optical depth, (2) intermediate scales ($\sim 1\text{--}5$ km or $3\text{--}10 \langle h \rangle$), where radiative roughening makes reflectivity fluctuations stronger than those of optical depth, and (3) small scales ($< \sim 1$ km or $1\text{--}3 \langle h \rangle$) where radiative smoothing makes reflectivity fluctuations weaker than those of optical depth. Regime 2 becomes more pronounced as absorption and solar zenith angle increase because both enhance the contrast between side-illuminated and shadowed portions of the cloud at scales where smoothing is no longer effective.

4.2. Effect of Cloud Top Height Variability

We now examine the impact on the power spectra of including cloud top height variations in our model clouds. All the cases with variable cloud top in this section have a mean

geometrical thickness $\langle h \rangle = 0.3$ km as the flat cloud. Three methods have been used to generate cloud top variability: (1) the superposition on the flat cloud of fractional Brownian motion height variability with parameter values controlling spatial correlations and variance $2/3$ and 0.04 , respectively [Marshak *et al.*, 1999]; (2) the constant volume extinction coefficient assumption $b_{\text{ext}} = \langle \tau \rangle / \langle h \rangle$, so that $h_i = \tau_i / b_{\text{ext}}$; and (3) the square root dependence of Loeb *et al.* [1998] $h_i = K \sqrt{\tau_i}$, with $K = 0.086$ to preserve $\langle h \rangle = 0.3$ km. Note that only method 1 produces cloud top height variations that are uncorrelated with optical depth. The other two methods give clouds where the optically thicker portions of the cloud are also thicker geometrically. The largest variation in cloud geometrical thickness is produced by method 2: the range is $0.06\text{--}1.08$ km. Method 3 gives a range of $0.14\text{--}0.59$ km, while method 1 generates a range of $0.20\text{--}0.41$ km. Obviously, if our cascade clouds are meant to represent marine stratocumulus capped under a temperature inversion, the milder cloud top variations of method 1 should be considered the more realistic of the three.

Figure 8 shows the nadir reflectivity power spectra for the flat and variable cloud top clouds for $\omega_0 = 1$ (Figures 8a and 8b) and $\omega_0 = 0.98$ (Figures 8c and 8d), for $\text{SZA} = 30^\circ$ (Figures 8a and 8c) and 60° (Figures 8b and 8d). Cloud top height variability has greater effect on the spectra when SZA is high. When scattering is conservative, flat and type 1 clouds have almost identical power spectra (both Sun angles) with little discernible intermediate scale roughening. Clouds with stronger cloud top variations produce pronounced roughening which begins at large scales. The most enhanced roughening is, as expected, for type 2 clouds. The slopes for small scales ($r < 1$ km) are, however, closer (e.g., slope ratio of type 2 over flat clouds is ~ 0.9 at $\text{SZA} = 60^\circ$) for all cases and steeper than those of the optical depth field, thus indicating that radiative smoothing remains present at both Sun angles regardless of cloud top variations. The flat and type 1 cloud power spectra become distinct and exhibit roughening signatures at intermediate scales only when scattering is nonconservative ($\omega_0 = 0.98$) and $\text{SZA} = 60^\circ$. Roughening is caused by low-order scattering events due to side illumination and shadowing. These effects become stronger for clouds with substantial geometric cloud variability (type 2 and 3 clouds) resulting in decorrelation of the reflectivity from the optical depth field. Even at $\text{SZA} = 30^\circ$, roughening is clearly discernible for $\omega_0 = 0.98$ and strong cloud top bumps. Therefore intermediate- and large-scale flattening of power spectra (more easily detectable at an absorbing band) may give a measure of bumpiness in cloud fields observed under appropriate conditions.

4.3. Effect of Cloud Fraction and Surface Albedo

The effects of cloud fraction and surface albedo on the appearance of power spectra are examined concurrently since they are directly coupled. Surface albedo is expected to make stronger contributions to the reflected radiation field when cloudy skies are interrupted by clear patches.

For a nonreflecting surface the power spectrum of a partially cloudy (pc) sky (cloud fraction 0.56) at $\text{SZA} = 45^\circ$ (labeled “pc_ $R_s = 0.0$ ” in Figure 9) looks generally similar to that of overcast sky (ovc). A closer examination, however, using regression in a $\log E_{\text{pc}}$ versus $\log E_{\text{ovc}}$ plot gave a slope ratio of 0.92 for conservative scattering, suggesting that fewer clouds produce less smoothing. For nonconservative scattering ($\omega_0 = 0.98$), replacing some of the cloudy columns with nonreflecting

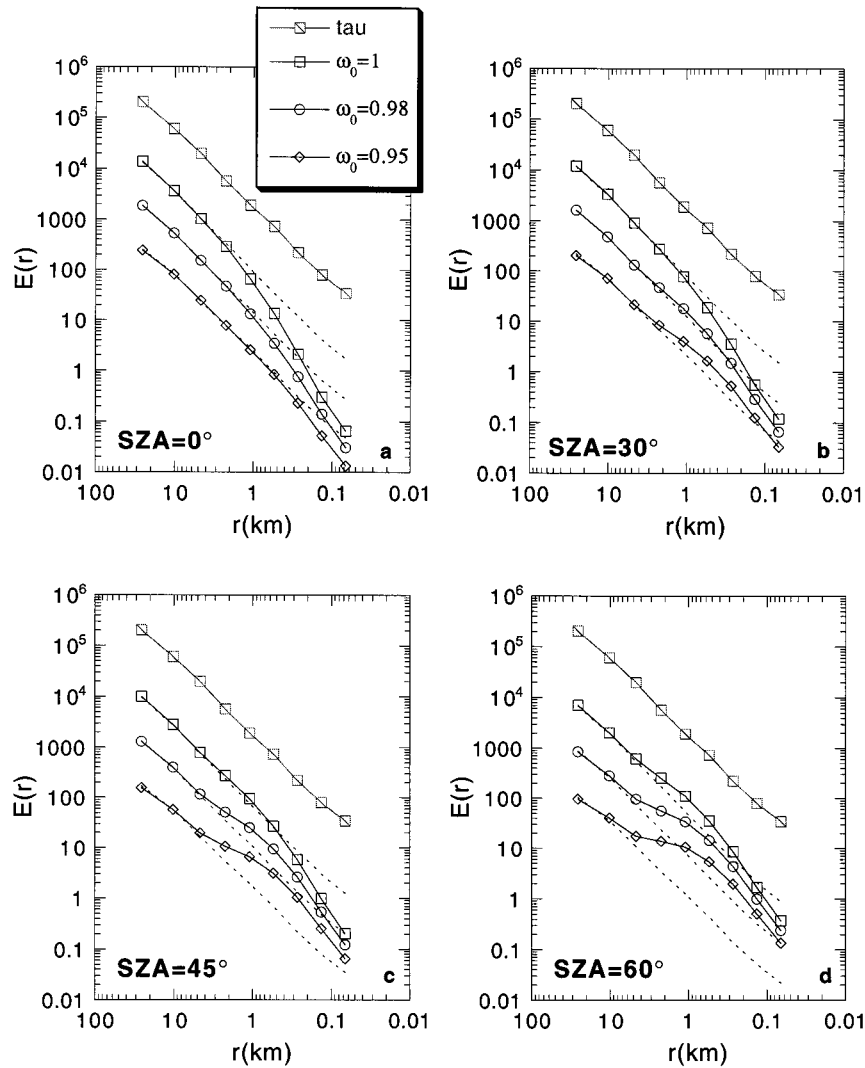


Figure 7. Octave-binned power spectra comparison for four solar zenith angles of (a) 0° , (b) 30° , (c) 45° , and (d) 60° and three different single scattering albedos as indicated in the legend. From MC simulations (solid lines, open symbols) and IPA calculations using DISORT (dotted lines, where decreasing spectral power corresponds to decreasing single scattering albedo) on the same cascade used in Figure 6.

(black surface) clear columns has a similar effect, but the presence of roughening makes a slope comparison less reliable. When the surface underlying the cloud is allowed to be reflective, the effects on the spectrum vary from insignificant (for surface reflectance $R_s = 0.1$ and $\omega_0 = 1$ in Figure 9a) to very dramatic ($R_s = 0.3$, $\omega_0 = 0.98$, CF = 0.56, SZA = 45° in Figure 9b, and $R_s = 0.5$, $\omega_0 = 0.99$, CF = 0.81, SZA = 30° , 60° in Figures 9c and 9d). The main feature introduced by strong surface reflection is decorrelation of optical depth from reflectivity at large and intermediate scales because regions of thick and thin clouds can have similar reflectivities, yielding extensive flattening of spectral slopes. A less extreme manifestation of this phenomenon seems to be present in the observations (see, for example, Figures 2a and 2c). We should stress, however, that the magnitude and extent of spectral flattening depend on the way clear breaks are introduced in the overcast model cloud. Here, clear breaks are created in the manner described by Marshak *et al.* [1999], which tends to generate clusters of contiguous clear columns (approximately following the observed power law behaviour of cloud number versus

size). Had the clear columns been modeled as “holes” in the cloud, so that clear and cloudy columns alternate with higher frequency, the flattening of the power spectra would have probably been tamer. Surface reflectance for partially cloudy skies therefore adds another element of complexity in the interpretation of observed spectra at large scales but leaves small scales unaffected as long as cloud cell sizes are significantly greater than a few photon mean free paths. The latter result is encouraging for remote-sensing methods such as inverse nonlocal IPA (NIPA) which corrects for the radiative smoothing at small scales.

4.4. Autocorrelations

MC simulations qualitatively reproduce the autocorrelation behaviour seen in the observations. This is shown in Figure 10, which summarizes the 10-column (=250 m) fixed lag and scale length (same as Figure 5) results of various MC experiments with clouds having a range of optical depths, geometrical thicknesses, cloud top variabilities, fractal and variance parameters, and Sun angles. Each point is the average of 10 autocorrelation

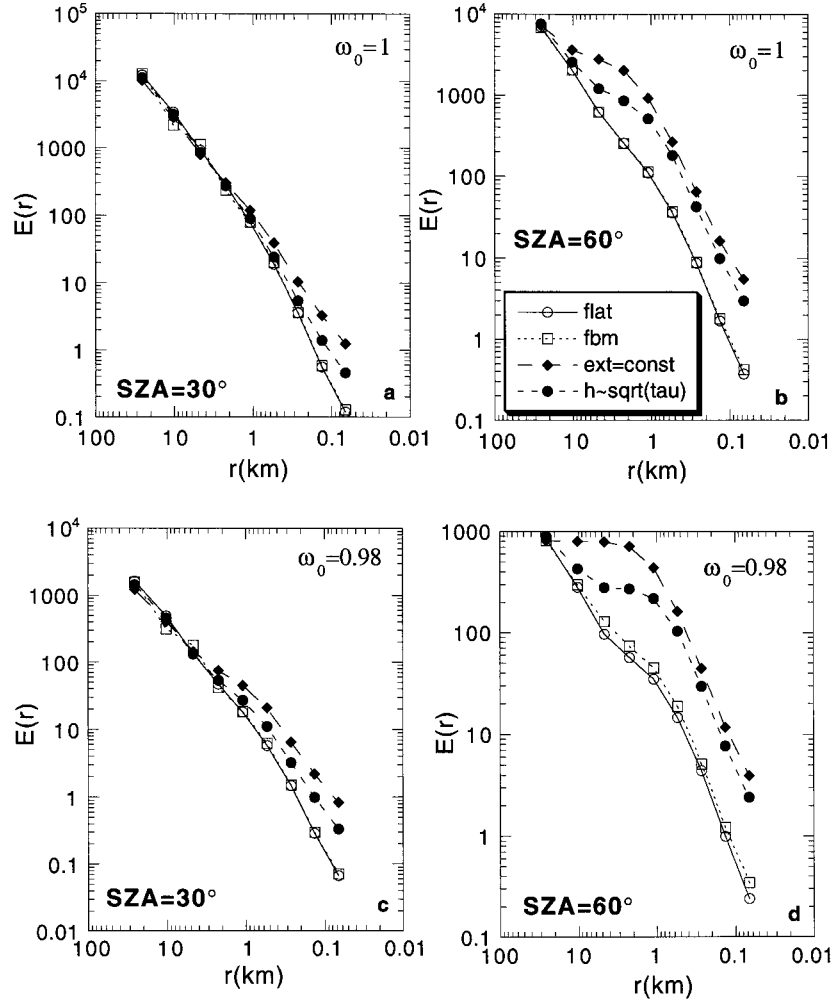


Figure 8. Comparison of MC-produced octave-binned power spectra for the cascade optical depth field of Figure 7 on which various types of cloud top variability were added as described in the text. fbm, type (1) variability; ext = const, type (2) variability; and $h \sim \sqrt{\tau}$, type (3) variability. SZA = 30° (Figures 8a and 8c) and 60° (Figures 8b and 8d); $\omega_0 = 1$ (Figures 8a and 8b) and 0.98 (Figures 8c and 8d).

functions (one for each realization). Moreover, because of the controlled conditions we can directly examine the effect of various factors on the autocorrelation statistics for conservative and non-conservative scattering.

The findings of the autocorrelation analysis for overcast clouds over a black surface can be summarized as follows (only the first can be deduced from Figure 10): (1) the autocorrelation function drops more rapidly in the presence of absorption, (2) the autocorrelation function drops more slowly at small SZA compared to large SZA, (3) the ratio of conservative to absorbing autocorrelation increases with SZA, (4) the autocorrelation function drops more slowly the milder the cloud top variability, and (5) the autocorrelation function drops more slowly the geometrically thicker the cloud. These results are consistent with those from the power spectra analysis for both observations and simulations. The systematic differences between autocorrelations at conservative and absorptive wavelengths can perhaps be used as the basis of a hyperspectral experiment searching for the wavelength dependence of unmodeled cloudy sky absorption. Such a study will provide another approach for investigating recent claims of unexplained absorption in the visible range [Cess *et al.*, 1999].

5. Use of Spectra to Evaluate Retrieval Methods

Virtually all current operational optical depth retrieval algorithms from satellite radiometric observations rely on IPA, which assumes that the observed pixel reflectivity depends only on the local optical properties of the pixel (no net radiative interaction among pixels). The MC simulation results of section 4 suggest that because of 3-D effects, scale-invariant optical depth fields (i.e., fields with straight-line power spectra in log-log plots) can produce reflectivity fields where the spectral slope changes with scale. Since IPA reflectivity power spectra have the same shape as those of optical depth (e.g., Figure 7), inversion of reflectivity fields with IPA-type methods results in retrieved optical depth spectra that follow closely those of reflectivity (i.e., spectra that do not obey the scale invariance of the actual optical depth fields). This is demonstrated in Figure 11: the spectra of optical depth retrieved with IPA bear a close resemblance to their counterparts of nadir reflectivity shown, for example, in Figure 7. Thus methods that improve retrievals over IPA by removing 3-D effects are needed. For high Sun, one such method is NIPA developed by Marshak *et al.* [1995]

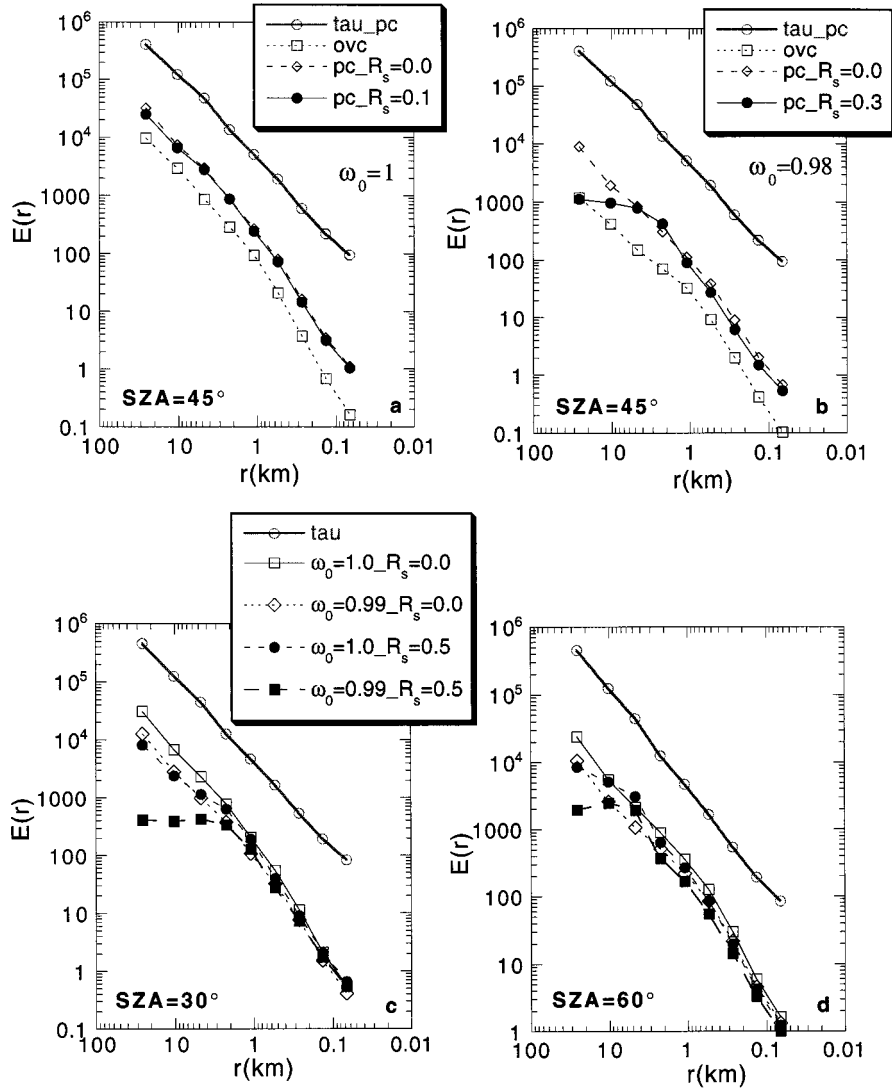


Figure 9. Comparison of MC-produced octave-binned power spectra for overcast (ovc) and partially cloudy (pc) with or without Lambertian surface reflectance (the value of albedo is indicated in all legends after the underscore). (a) and (b) SZA = 45°, cloud fraction (CF) = 0.56; $\omega_0 = 1$ (Figure 9a), $\omega_0 = 0.98$ (Figure 9b); $\langle h \rangle = 0.5$ km, type 1 cloud top variability with parameter values for spatial correlation and variance 2/3 and 0.05, respectively. (c) and (d) SZA = 30° and SZA = 60°, respectively (legend is for both), with CF = 0.81, $\langle h \rangle = 0.3$, type 1 cloud top variability with parameter values for spatial correlation and variance 2/3 and 0.02, respectively. Cloud base is at 1 km for all experiments.

and modified for the retrieval (inverse) problem by *Marshak et al.* [1998a]. In the direct problem (estimation of reflectivity field from optical depth), NIPA introduces small-scale smoothing to IPA, while in the inverse problem (retrieval of optical depth from a reflectivity field), NIPA roughens the field to bring it closer to IPA. For low Sun a correction method where IPA retrievals use the dimensionless index normalized difference of nadir reflectivity (NDNR) instead of a single-band reflectivity was suggested by *Oreopoulos et al.* [2000]. This method smoothes the intermediate-scale roughening prevalent at low Sun illuminations.

The power spectra resulting from two versions of inverse NIPA are shown in Figure 11a. The first (labeled NIPA) applies the NIPA roughening kernel on the MC reflectivities and then retrieves optical depths as in IPA; the second (labeled NIPA_tau) applies the roughening kernel on the optical depth field inferred by IPA inversion of MC reflectivities. In both

cases the parameters of the NIPA kernel were selected so as to minimize the rms error in optical depth. NIPA restores the true optical depth power spectrum at all but the smallest scales, and works slightly better for the NIPA_tau case. For SZA = 60°, retrievals using NDNR and a NIPA-NDNR combination intended to also roughen small-scale smoothing are used. For this particular exercise,

$$\text{NDNR} = \frac{R(\omega_0 = 1) - R(\omega_0 = 0.98)}{R(\omega_0 = 1) + R(\omega_0 = 0.98)}. \quad (4)$$

NDNR is less successful, removing the roughening at ~ 2 km but also infusing some smoothing between 0.5 and 1 km, absent in the standard IPA retrieval. The NIPA-NDNR retrieval is too smooth below 1 km but performs very well above that scale. Thus not only do NIPA, NDNR, and NIPA-NDNR retrievals produce better optical depth statistics (e.g., minimum, maximum, mean, higher-order moments) than IPA, as shown by

Oreopoulos *et al.* [2000] but also improve the scale-by-scale variability of the retrieved optical depth field. These methods therefore merit attention as alternatives to IPA for high-resolution retrievals.

6. Summary and Conclusions

We have performed an extensive analysis of observed (Landsat Thematic Mapper) and simulated (Monte Carlo) spatial power spectra for high-resolution shortwave nadir reflectivities in cloudy conditions. We have shown that the power spectra take a variety of shapes and forms, depending on wavelength (conservative versus absorbing), illumination geometry, cloud top variability, and perhaps other variables, thus providing a basis for interpreting observed spectra. We have suggested that efficient spectral intercomparisons are achieved by means of log-log slopes, derived from linear least squares regression, and logarithmic scatterplots of one spectrum versus another. We have pointed to characteristic features in the spectra that may potentially be used to guide the choice of appropriate retrieval methods for particular situations and shown that spectra can be used to evaluate the performance of these methods for scale-invariant cloud fields.

We have demonstrated that under certain conditions, TM spectra can be affected by both radiative “roughening” at intermediate scales (1–5 km), being more prevalent at large solar zenith angles, and radiative “smoothing” at small scales (<1 km) as documented in previous studies. These processes

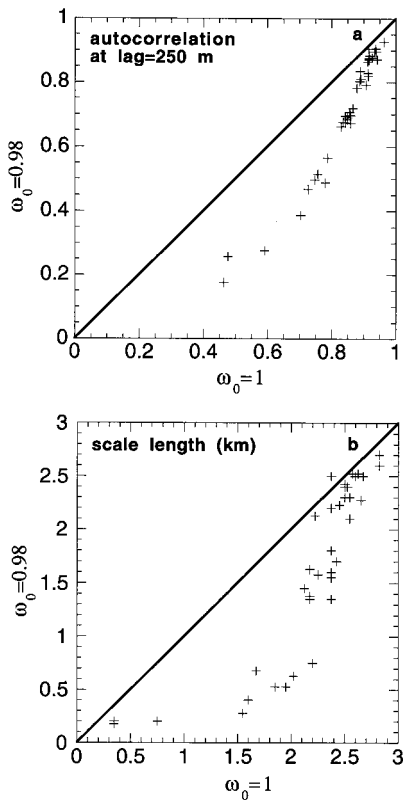


Figure 10. Same as Figure 5 but for 38 MC experiments (each experiment consists of 10 realizations) with overcast clouds of different characteristics and illuminated by SZAs = 0°, 30°, 45°, and 60°. The fixed lag is 250 m (10 columns). Surface is black.

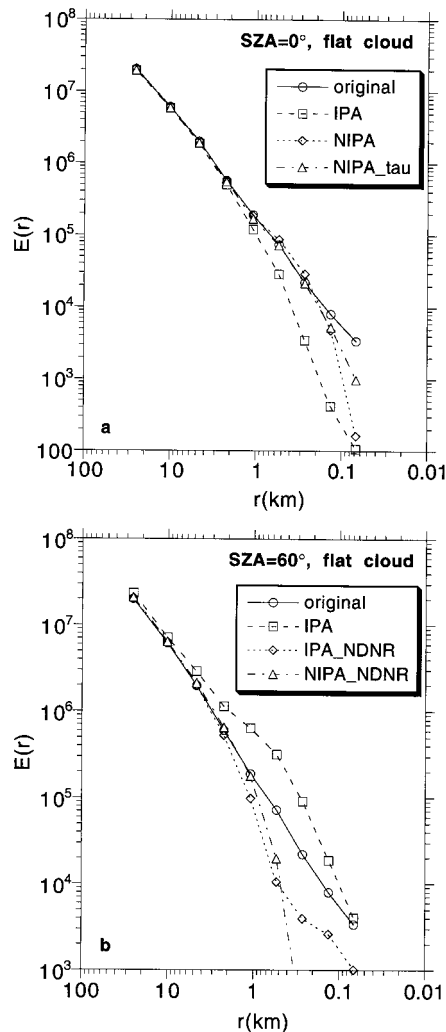


Figure 11. Comparison of true (original) and retrieved (by inverting MC reflectivities) octave-binned optical depth spectra (b) using standard IPA, NDNR, and NIPA-NDNR for SZA = 60° or (a) IPA and two versions of NIPA (see text) for SZA = 0°. NIPA parameters were selected so as to minimize the rms difference from the true optical depth field.

proved to be wavelength-dependent, with systematic differences between conservative TM band 4 (~0.8 μm) and absorbing band 7 (~2.2 μm) and with band 7 exhibiting more roughening and less smoothing. The reduced band 7 smoothing at small scales was also confirmed by the faster decrease with distance of the autocorrelation function for this band compared to band 4. MC reflectivity spectra were also used to illustrate that the scale break for radiative smoothing moves toward lower values with more absorption and that radiative roughening increases with increasing absorption and solar zenith angle. The shape of the power spectra were shown to be sensitive to the magnitude and type of cloud top height variability, which largely controls side illumination and shadowing and (in the case of partially cloudy skies) the presence of surface reflectance. The spectral signatures of decorrelation between reflectance and optical depth at large scales became stronger as the magnitude of cloud top variations and surface albedo increased. The small-scale smoothing, however, persisted in all cases. The autocorrelation analysis for MC simu-

lations was consistent with our understanding of radiative transfer and in general agreement with the corresponding observational analysis.

There is a growing awareness among scientists who are involved in the remote sensing of cloud properties that regional means are not adequate for characterizing cloud fields or as building blocks for parameterizations in climate models. A step in the right direction is the provision of histograms and higher-order moment cloud products from the Moderate-Resolution Imaging Spectroradiometer (MODIS) instrument flying aboard the Terra platform of the EOS mission. These products, however, may be biased because of unaccounted for 3-D radiative effects. Power spectra are a compact means for quantitatively characterizing 3-D effects and deriving parameters for various correction methods such as NIPA and NIPA-NDNR. It may therefore be valuable, given the projected increase in computational power, that spatial Fourier power spectra calculated with fast Fourier transform algorithms be included in the list of future operational products in cloudy regions.

Acknowledgments. We would like to thank P. Austin, H. Barker, A. Davis, F. Evans, R. Pincus, S. Platnick, T. Várnai, and W. Wiscombe for helpful discussions. This research was supported by funding provided under Landsat Science Team activities, which is part of NASA-MTPE, under proposal 1996-MTPE-00116, the Department of Energy's ARM program under grants DE-A102-97ER62369 and DE-A105-90ER61069, and NASA grant NAG5-6675 as part of the EOS validation program.

References

- Barker, H. W., and J. A. Davies, Cumulus cloud radiative properties and the characteristics of satellite radiance wavenumber spectra, *Remote Sens. Environ.*, **42**, 51–64, 1992.
- Barker, H. W., and D. Liu, Inferring optical depth of broken clouds from Landsat data, *J. Clim.*, **8**, 2620–2630, 1995.
- Cahalan, R. F., and J. B. Snider, Marine stratocumulus structure, *Remote Sens. Environ.*, **28**, 95–107, 1989.
- Cahalan, R. F., W. Ridgway, W. J. Wiscombe, T. L. Bell, and J. B. Snider, The albedo of fractal stratocumulus clouds, *J. Atmos. Sci.*, **51**, 2434–2455, 1994.
- Cess, R. D., M. H. Zhang, F. P. J. Valero, S. K. Pope, A. Bucholtz, B. Bush, C. S. Zender, and J. Vitko, Absorption of solar radiation by the cloudy atmosphere: Further interpretation of collocated aircraft measurements, *J. Geophys. Res.*, **104**, 2059–2066, 1999.
- Chambers, L. H., B. A. Wielicki, and K. F. Evans, Accuracy of the independent pixel approximation for satellite estimates of oceanic boundary layer cloud optical depth, *J. Geophys. Res.*, **102**, 1779–1794, 1997.
- Davis, A., A. Marshak, W. J. Wiscombe, and R. F. Cahalan, Scale invariance of liquid water distributions in marine stratocumulus, part I, Spectral properties and stationarity issues, *J. Atmos. Sci.*, **53**, 1538–1558, 1996.
- Davis, A., A. Marshak, R. F. Cahalan, and W. J. Wiscombe, The Landsat scale break in stratocumulus as a three-dimensional radiative transfer effect: Implications for cloud remote sensing, *J. Atmos. Sci.*, **54**, 241–260, 1997.
- Loeb, N. G., and R. Davies, Observational evidence of plane parallel model biases: Apparent dependence of cloud optical depth on solar zenith angle, *J. Geophys. Res.*, **101**, 1621–1634, 1996.
- Loeb, N. G., T. Várnai, and D. M. Winker, Influence of subpixel-scale cloud-top structure on reflectances from overcast stratiform cloud layers, *J. Atmos. Sci.*, **55**, 2960–2973, 1998.
- Marshak, A., A. Davis, W. J. Wiscombe, and R. F. Cahalan, Radiative smoothing in fractal clouds, *J. Geophys. Res.*, **100**, 26,247–26,261, 1995.
- Marshak, A., A. Davis, R. F. Cahalan, and W. J. Wiscombe, Nonlocal independent pixel approximation: Direct and inverse problems, *IEEE Trans. Geosci. Remote Sens.*, **36**, 192–205, 1998a.
- Marshak, A., A. Davis, W. J. Wiscombe, and R. F. Cahalan, Radiative effects of sub-mean-free-path liquid water variability observed in stratiform clouds, *J. Geophys. Res.*, **103**, 19,557–19,567, 1998b.
- Marshak, A., A. Davis, L. Oreopoulos, W. J. Wiscombe, and R. F. Cahalan, On the removal of the effect of horizontal fluxes in two-aircraft measurements of cloud absorption, *Q. J. R. Meteorol. Soc.*, **125**, 2153–2170, 1999.
- Oreopoulos, L., A. Marshak, R. F. Cahalan, and G. Wen, Cloud power spectra—Dependence on solar zenith angle and wavelength, implications for cloud optical property retrievals, paper presented at 10th AMS Conference on Atmospheric Radiation, Am. Meteorol. Soc., Madison, Wis., June 28 to July 2, 1999.
- Oreopoulos, L., R. F. Cahalan, A. Marshak, and G. Wen, A new normalized difference cloud retrieval technique applied to Landsat radiances over the Oklahoma ARM site, *J. Appl. Meteorol.*, in press, 2000.
- Platnick, S., Approximations for horizontal photon transport in cloud remote sensing problems, *J. Quant. Spectrosc. Radiat. Transfer*, in press, 2000.
- Stamnes, K., S.-C. Tsay, W. J. Wiscombe, and K. Jayaweera, Numerically stable algorithm for discrete-ordinates-method radiative transfer in multiple scattering and emitting layered media, *Appl. Opt.*, **27**, 2502–2509, 1988.
- Várnai, T., Influence of three-dimensional radiative effects on the spatial distribution of shortwave cloud reflection, *J. Atmos. Sci.*, **57**, 216–229, 2000.
- Wielicki, B. A., R. D. Cess, M. D. King, D. A. Randall, and E. F. Harrison, Mission to planet Earth: Role of clouds and radiation in climate, *Bull. Am. Meteorol. Soc.*, **76**, 2125–2153, 1995.
- Zuidema, P., and K. F. Evans, On the validity of the independent pixel approximation for boundary layer clouds observed during ASTEX, *J. Geophys. Res.*, **103**, 6059–6074, 1998.

R. F. Cahalan, A. Marshak, L. Oreopoulos, and G. Wen, NASA GSFC, Code 913, Greenbelt, MD 20771. (cahalan@climate.gsfc.nasa.gov; marshak@climate.gsfc.nasa.gov; lazarus@climate.gsfc.nasa.gov; wen@climate.gsfc.nasa.gov)

(Received August 11, 1999; revised February 23, 2000; accepted February 24, 2000.)